Local structural coupling of A- and B-site disorder in perovskite bismuth-based piezoelectrics

Bo Jiang[1], De-Ye Lin[2], Tor Grande[1] and Sverre M. Selbach[1*]

[1]Department of Materials Science and Engineering,

NTNU – Norwegian University of Science and Technology, 7491 Trondheim, Norway.

[2]Institute of Applied Physics and Computational Mathematics, Fenghao East Road 2, Beijing 100094, P.R. China

*Correspondence should be addressed to selbach@ntnu.no

Abstract

The local and average structure of (1-x)$Bi_{0.5}K_{0.5}TiO_3$-$x$$BiFeO_3$ (BKT-xBFO, x = 0.25 and 0.5) solid solutions are studied by synchrotron X-ray total scattering from ambient to 773 K. Pair distribution functions (PDFs) demonstrate that disordered BKT-0.25BFO and BKT-0.5BFO show the same structural coherence length of ~16 Å as pure $Bi_{0.5}K_{0.5}TiO_3$, while their average structures are pseudocubic at all temperatures. Complementary density functional theory (DFT) calculations suggest distinctly different local structural distortions in BKT-0.25BFO and BKT-0.5BFO with random cations distribution on both A- and B-lattice. Based on the experimental and theoretical analysis, we propose that the optimal piezoelectric properties found at the structural phase boundary composition of x = 0.25 originate from tetragonal and rhombohedral polar nanoregions (PNRs) in an on average pseudocubic matrix. In contrast, for x = 0.5 there are only pseudorhombohedral polar distortions in a pseudocubic matrix phase.

1. INTRODUCTION

Bismuth-based solid solutions like (1-*x*)$Bi_{0.5}K_{0.5}TiO_3$-*x*$BiFeO_3$ (BKT-*x*BFO) [1-9] are being developed as alternatives to lead-containing and environmentally hazardous PZT-based ($PbZr_{1-x}Ti_xO_3$) materials [10, 11] for piezoelectric and electromechanical applications. $BiFeO_3$ (BFO) is multiferroic with high Néel (T_N) and Curie (T_C) temperatures of 370 °C and 830 °C, respectively, and the rhombohedral *R*3*c* structure [12-15] displays a large spontaneous polarization, *Ps*, of ~90μC/cm^2 at room temperature [16-21]. $BiFeO_3$ is a displacive ferroelectric with strong long-range order and structural coherence, and only one type of atoms at each Wyckoff site. In contrast, $Bi_{0.5}K_{0.5}TiO_3$ (BKT) has two different cations on the A-site, K^+ (r = 1.65 Å, coordination number = 12) and Bi^{3+} (r =1.31 Å, CN extrapolated to 12 [22]). K^+ and Bi^{3+} show a size difference of 21% and the latter possesses a 6*s*^{2} lone pair. Relaxor-like BKT is a ferroelectric with tetragonal *P*4*mm* structure at room temperate, a reported T_C of 370-410 °C [10, 23-26] and a second phase transition at a temperature T_2 in the range of 270-310 °C [10, 23, 24, 27, 28]. Temperature-dependent structural studies have shown that BKT is structurally disordered at all temperatures, but the coherence length, over which the lattice is structurally ordered, increases upon cooling [29]. The structural coherence length in a displacive ferroelectric corresponds to the domain size, while in a ferroelectric relaxor it is defined by the size of polar nanoregions.

The solid solutions BKT-*x*BFO show promising dielectric and piezoelectric properties [30, 31], with maximum dielectric and piezoelectric properties found close to x≈0.25 in BKT-*x*BFO where the structure is pseudocubic from X-ray diffraction [7, 8]. Compared to their end members, solid solutions of BKT and BFO avoid the phase purity and processing issues hampering the preparation of high-quality BKT and BFO ceramics [23, 24, 32]. With rhombohedral and tetragonal end members, a structural phase boundary is anticipated close to

x≈0.25, possibly with polar tetragonal nanodomains in a pseudocubic matrix [7]. A morphotropic phase boundary (MPB) has also been reported for $x = 0.6$ [4], while relaxor-like behavior and pseudocubic structure was found for x = 0.4-0.6 [30, 31]. A microscopic understanding of why the dielectric and piezoelectric properties display a maximum value at x = 0.25, even when the MPB is found around x = 0.6, is however missing. While $PbZr_{1-x}Ti_xO_3$ has solid solution and chemical disorder on the perovskite B-site sublattice [33, 34], and $Na_{0.5}Bi_{0.5}TiO_3$-$x$$BaTiO_3$(NBT–$x$BT) on the A-site sublattice [35-37], BKT-xBFO has solid solution and chemical disorder on both the A- (Bi^{3+} and Bi^{3+}/K^{+}) and the B-site (Ti^{4+} and Fe^{3+}) sublattices, implying a more complex and disordered material system.

The local structure and relaxor-like behavior of BKT-xBFO may arise from A or B-site cation disorder, as found for the BKT end member [29, 38]. In BKT below T_C, local polar regions are partly disordered and the spatially averaged macroscopic polarization is smaller than that found on the local scale. Above T_C, the local polar regions prevail, but are now completely disordered and the macroscopic polarization levels to zero [29]. As for displacive ferroelectric $BiFeO_3$ [16, 19], the average structure of BKT also appears to go through a displacive transition at T_C, while the local structure shows order-disorder characteristics. The microscopic mechanisms of ferro- and piezoelectricity in the BKT-xBFO system are unknown.

Pair distribution functions (PDFs) from total scattering can reveal both the local and intermediate range structure of disordered crystalline solids through synchrotron X-ray or neutron scattering, and has been applied with great success to numerous piezoelectrics [39-45] and relaxor ferroelectrics [46-48]. A limitation of synchrotron X-ray PDFs is the low X-ray scattering strength of oxygen, particularly compared to heavy elements like bismuth. Combining synchrotron X-ray PDFs with density functional theory (DFT) calculations to optimize the local environments of oxygen ions can thus give more realistic structural models.

Here, we combine temperature-dependent synchrotron X-ray pair distribution functions (PDFs) with DFT calculations to study the local and average structure of BKT-xBFO (x = 0.25, 0.5). We find distinctly different local structural distortions for the composition with optimal piezoelectric properties, BKT-0.25BFO, from those observed for pseudocubic BKT-0.50BFO and tetragonal BKT [29]. The agreement between total scattering experiments and DFT calculations on BKT-xBFO in this work demonstrates the potential for unravelling structure-property relationships in materials with disordered structures and complex chemical compositions.

2. EXPERIMENTAL AND COMPUTATIONAL DETAILS

Powder samples with compositions (1-x)$Bi_{0.5}K_{0.5}TiO_3$-$x$$BiFeO_3$ x=0.25 and 0.5 were prepared by conventional solid state reaction using dried Bi_2O_3 (99.9%; Aldrich), K_2CO_3 (99.99%; Aldrich), TiO_2 (99.9%; Aldrich) and Fe_2O_3 (99.98%; Aldrich) [29, 38]. Synchrotron X-ray total scattering was performed at beamline ID22 (λ = 0.199965 Å, 62 keV) at the European Synchrotron Radiation Facility (ESRF). Rietveld refinement of reciprocal space diffraction patterns was done with the General Structure Analysis System (GSAS) program [49]. Pair distribution functions (PDFs) G(r) were obtained with the PDFgetX3 software [50] using a Q_{max} of 22.8 $Å^{-1}$. PDFs were analyzed both by small-box modeling using PDFgui [51] and by large-box modeling by Reverse Monte Carlo (RMC) simulations using RMCprofile [52]. The parameters obtained from the Rietveld refinements were used as starting parameters in PDFgui modeling. Lattice constants, atomic positions and atomic displacement parameters (ADP) were refined and the cutoff radius for quadratic atomic correlations was set to 5 Å to improve the fit in the low-r range. For the pseudocubic model, the a, b and c lattice parameters were fixed to the same value to avoid tetragonal distortions. Reverse Monte Carlo (RMC) fitting of PDFs

were performed with the RMCprofile software [52] using a 12×12×12 supercell containing 8640 atoms. At least 2.0×10^6 atomic moves were generated per simulation. The initial structures were obtained from Rietveld refinement with the *P*4*mm* structure for BKT, and cubic structures for BKT-0.25BFO and BKT-0.5BFO. Finally, the RMC model was obtained by fitting PDF G(r), scattering function F(Q) and the X-ray Bragg peaks simultaneously. In the RMC simulations bond valence sum (BVS) restrictions were applied to avoid unphysical bond lengths. Bi^{3+} and K^{+} were allowed to swap places on the A sublattice, and Fe^{3+} and Ti^{4+} on the B sublattice.

Density functional theory (DFT) calculations were carried out with the *Vienna Ab initio Simulation Package* (VASP) code [53, 54] using the PBEsol functional [55, 56] and the standard PBE PAW potentials Bi_d ($5d^{10}6s^26p^3$), K_sv ($3s^23p^654s^1$), Ti_pv ($3p^63d^24s^2$), Fe_pv ($3p^63d^74s^1$) and O ($2s^2p^4$) supplied with VASP. Brillouin zone integration was done on a 3×3×3 k-mesh for 40-atoms perovskite cells in this work. Plane waves were expanded up to a cutoff energy of 550 eV and the atom positions and lattice vectors were relaxed until the forces on the atoms were less than 0.001 eV/Å. The magnetic order on the Fe sublattice was initialized as either G-type or A-type collinear antiferromagnetism, and a Hubbard U value of 4 eV was applied to the Fe 3d states [57, 58]. The spontaneous polarization P_s for the supercells were calculated by the point charge method as the Berry phase method [59] would require a centrosymmetric reference state which would be artificial in these disordered supercells.

3. RESULTS AND DISCUSSION

3.1 Experimental PDF Modeling

Reciprocal space synchrotron X-ray diffraction patterns of BKT-*x*BFO (*x*=0.25, 0.5, herafter referred to as BKT-0.25BFO and BKT-0.5BFO, respectively) powders collected from 300 to 773 K can be indexed as cubic perovskite structure (Supplementary Information Figure S1). To investigate the local structure, temperature dependent PDFs G(r)s are displayed in Figure 1, with the PDFs of pure BKT [29] included for comparison in Figure 1a. The PDFs of all three compositions show very similar evolution with increasing temperature, where the peak broadening is dominated by increasing thermal motion. The ticks in Figure 1a indicate the major bond distance peaks for the tetragonal BKT structure. The first two green ticks around 3.5 Å represent the Bi/K-Ti short and long bonds, respectively, resulting from polar Ti displacements along the z-axis. Both BKT-0.25BFO and BKT-0.5BFO have very similar local structures compared to BKT, which suggests that the origin of ferroelectric polarization does not change with increasing $BiFeO_3$ content. The cubic perovskite structure should display only one peak for A-B bonds (Figure 1(b)), while rhombohedral *R*3*c* $BiFeO_3$ should display four peaks around 3-3.8 Å [58] from the relative displacement of Fe^{3+} with respect to Bi^{3+} (Figure 1(c)). The local structure of BKT-0.25BFO and BKT-0.5BFO clearly cannot be described by a simple space group model, and this is attributed to a strongly disordered local structure.

To further study the local and intermediate range structure we use small-box modeling with PDFgui to fit different *r*-ranges for BKT-0.25BFO and BKT-0.5BFO with the mixed A-site average *P*4*mm* and the pseudocubic structure models at room temperature, as shown in Figure 2, where BKT [29] is included for comparison. Note that the high-*r* region describes the average structure better than the low-*r* region, highlighting the difference between the local and average structure. The *P*4*mm* average structure model provides a much better description

of pure BKT than the pseudocubic model, as seen in Figure 2a and 2b [29, 38]. The reliability factors R_w in Figure 2c and 2d for the BKT-0.25BFO patterns suggest that the *P*4*mm* average structure is more suitable to describe the local structure below r < 10 Å, while the structure for the *r*-range from 10 Å to 30 Å is better described by a pseudocubic model. The main deviation from the crystallographic models for the local structure comes from the two Bi/K-T bond distances around 3~4 Å (Figure 2c). This suggests that the local structure of BKT-0.25BFO is similar to the *P*4*mm* structure, while local tetragonal distortions partly cancel each other in the intermediate *r*-range. The reliability factors R_w for BKT-0.5BFO differ strongly from BKT-0.25BFO, where both fitted *r*-regions shown in Figure 2f are better described by the pseudocubic model than the *P*4*mm* average structure model (Figure 2e).

To shed further light on the effect of $BiFeO_3$ addition to $Bi_{0.5}K_{0.5}TiO_3$ we investigate the local and intermediate structure by comparing the PDF patterns of the three compositions at 300 and 773 K in Figure 3 (more details and plots can be found in Figures S2-5 in the Supporting Information). The BKT and BKT-0.25BFO PDF patterns at 300 K in Figure 3a are very similar below *r* ~16 Å. Beyond r ~16 Å, the PDFs of BKT and BKT-0.25BFO show distinct differences at 300 K, with increasing deviations towards higher *r*. In contrast, at 773 K the PDFs of BKT and BKT-0.25BFO are very similar across the whole plotted *r*-range, Figure 3b. A possible explanation is that 773 K is above the Burns temperature T_D of BKT, implying that the presence of polar nanoregions (PNRs) below T_D leads to distinctly different intermediate range structures.

Comparing the BKT-0.25BFO and BKT-0.5 PDF patterns in Figures 3c and 3d, it is evident that the local and intermediate range structures are more similar at 300 K than the BKT and BKT-0.25BFO PDFs at the same temperature (Figure 3a). The PDFs collected at 773 K are very similar across the whole plotted r-range, also implying that the intermediate ranger

structure of BKT and BKT-0.5BFO also are very similar at 773 K. To investigate if the local and intermediate range structure of BKT-0.25BFO, the composition with optimal piezoelectric properties, can simply be understood as a linear combination of the BKT and BKT-0.5BFO structure, we compare the measured BKT-0.25BFO PDFs with the weighted averages of the BKT and BKT-0.5BFO PDFs in Figures 3e and 3f. Despite some deviations in peak intensities in the intermediate range region, the measured BKT-0.25BFO PDF is remarkably similar to the weighted average of the PDFs of tetragonal BKT and pseudocubic BKT-0.5BFO. This indicates that the structure of BKT-0.25BFO can be understood as a mixture of tetragonal and pseudocubic local regions, as proposed by Morozov *et al*. [7]. We note that the differences between the PDF patterns at 300 and 773 K in Figure 3 resemble the order-disorder structure transition observed in pure BKT [29, 38], $BaTiO_3$ [60], nanocrystalline $BiFeO_3$ [42] and PZN-*x*PT [61].

3.2 DFT Simulations of Local Structure

DFT simulations were done to better understand the local structural disorder in the BKT-*x*BFO (*x*=0.25, 0.5) system. The total energies of the different Ti/Fe-ordering configurations, with alternating adjacent Bi and K, are shown in Figure 4 for pseudocubic structures of BKT-0.5BFO ($Bi_{0.75}K_{0.25}Ti_{0.5}Fe_{0.5}O_3$). All the geometry optimized configurations are named according to convention introduced by Gröting and Albe [62, 63]. Both A-type and G-type collinear antiferromagnetic ordering of Fe^{3+} magnetic moments [57] were considered in this work, and the 111 and all3+1 configurations have antiferromagnetic order as labelled in Figure 4(a). With A-type ordering, the total energy difference was 0.042 eV (4.05 kJ/mol) per formula unit of BKT-0.5BFO, with 001 and 110 being the most and least stable configurations. For G-type magnetic order, which is more stable than A-type, 001 is the most stable, while the 111

rock salt ordering is the least stable configuration, with a total energy difference of 0.055 eV (5.31 kJ/mol) per formula unit. Cation ordering will only be stable if the total enthalpy difference between the two most stable configurations is larger than the energy contribution from the entropy of mixing. This entropic energy contribution is of course temperature dependent, and the relevant temperature could be either the sintering temperature or the temperature where cation transport effectively freezes in as the system changes from an ergodic to a non-ergodic state [64]. If we for simplicity assume that the BKT-0.5BFO system is a regular solution [65] and consider both the A and B-site sublattice, the configurational mixing entropy a for two sub-lattice system $M1_xM2_{(1-x)}$ $N1_yN2_{(1-y)}$ is equal to that of an ideal solution [66]: $\Delta S_{mix} = -R[x\cdot\ln(x)+(1-x)\ln(1-x) + y\cdot\ln(y)+(1-y)\ln(1-y)]]$.

For BKT-0.5BFO ($Bi_{0.75}K_{0.25}Ti_{0.5}Fe_{0.5}O_3$), the entropy of mixing is thus $\Delta S_{mix(BKT\text{-}0.5BFO)}$ = 10.438J/(mol.K). At the sintering temperature of typically 1060 °C (1330 K), the energy contribution from configurational entropy $T\Delta S_{mix,(BKT\text{-}0.5BFO)}$ is ~13.9 kJ/mol, and thus about three times higher than the enthalpy difference between two most stable configurations. Further investigation of the standard Gibbs free energy of mixing from a regular solution model in Figure S6 also show a value of -5.8 ± 2.97 kJ/mol at 1330 K. A positive Gibbs free energy of mixing, which would be required for cation ordering, is only found for temperatures too low to allow the necessary cation mobility for ordering to occur. These results strongly suggest that both the A- and B-site cation sublattices in real BKT-*x*BFO materials will be disordered with random local cation configuration.

We have summarized the unit cell tetragonality c/a of the fully relaxed configurations and the resulting polarization in all cases for BKT-0.25BFO and BKT-0.5BFO in Figure 5. In a 2×2×2 cell of BKT-0.25BFO there are three different arrangements for both the A-site and B-site, and a total of 18 configurations for the pseudocubic structure. We note that most of these

configurations show larger tetragonality than the average structure, suggesting that there are local regions with enhanced tetragonality and polarization. Some of the relaxed configurations, especially for the K-(11) group, show less tetragonality and can be considered pseudocubic with antiferrodistortive rotations of the octahedra, resulting in a pseudorhombohedral structure with $a^-b^-c^-$ tilt system. The *x*-, *y*- and *z*- components as well as the net local polarization in BKT-0.25BFO calculated from point charge for different configurations also support this interpretation of the structure. As all the configurations of the 2×2×2 BKT-0.5BFO cell in Figure 5(b) display a small tetragonality, we infer that the local structure is pseudocubic. Closer inspection of the final structures after geometry optimization shows that the relaxed 2×2×2 BKT-0.5BFO cells are pseudorhombohedral with antiferrodistortive octahedral rotations. Our presented DFT results (Figure 5) are consistent with the experimental room temperature PDFs in Figure 2. While the local structures of BKT-0.25BFO and BKT-0.5BFO show distinct differences, both compounds display a structural coherence length of about ~16Å, as also found pure BKT [29].

3.3. Reverse Monte Carlo Modeling

As the small-box modeling with PDFgui presented in Figure 2 did not give good fits to the local structure, we turn to large-box reverse Monte Carlo (RMC) modeling. Now, much better fits to the experimental PDFs of BKT, BKT-0.25BFO and BKT-0.5BFO are achieved, as shown in Figure 6(a-c). We focus now on the Bi partial PDFs in Figure 6(d-f) as they dominate the total PDFs due to the high X-ray scattering strength, and as the Ti-Ti partial PDFs in BKT and Fe-Fe partial PDFs in BFO show no significant differences in the low r-range (Figure S7 and Figure S8). The asymmetric Bi-Bi bonds represented by double peaks at ~3.9 Å arise from the tetragonal distortion of BKT and BKT-0.25BFO, while only one broad peak is observed

for BKT-0.5BFO (Figure 6(d)). The Bi-Ti(Fe) peaks in Figure 6(e) (Figure 6(f)) and stem from the polar Ti^{4+}(Fe^{3+}) displacements relative to the Bi^{3+} sublattice, and there are two main peaks at ~3.5 Å for all compositions due to local tetragonal distortion. The single peak at ~6.5 Å splits into a doublet due to the rhombohedral distortion, which emerges with increasing $BiFeO_3$ content. This observation suggests that both polar tetragonal and polar rhombohedral or monoclinic regions are present in BKT-0.25BFO at the local scale, and that these regions partly cancel each other at larger length scales. We thus infer tetragonal and rhombohedral polar nanoregions (PNRs) in a pseudocubic average matrix phase for BKT-0.25BFO, and a local structure with polar rhombohedral distortions in a pseudocubic average matrix phase for BKT-0.50BFO. The local structural differences from BKT (tetragonal) through BKT-0.25BFO (tetragonal and rhombohedral) to BKT-0.50BFO (rhombohedral) is analogous to the average structure variation from $PbTiO_3$ (tetragonal) across the MPB (monoclinic or tetragonal/rhombohedral) and into the Zr-rich region of $PbZr_{1-x}Ti_xO_3$ (rhombohedral). Based on a combination of DFT calculations and RMC modelling, our proposed local and mesoscopic polar vector models for BKT, BKT-0.25BFO and BKT-0.50BFO are shown in Figure 7. Here we illustrate the local and average structure of BKT-*x*BFO solid solutions with both A and B-sites disorder as well as how the polar vectors change with composition from relaxor-like BKT to non-relaxor $BiFeO_3$.

4. CONCLUSIONS

In summary, a combination of synchrotron X-ray total scattering and DFT calculations, with thermodynamic considerations, has been used to analyze local structural disorder from A and B-site disorder in BKT-*x*BFO (*x*=0.25, 0.5) solid solutions. The structural coherence persists up to ~16Å for BKT-0.25BFO and BKT-0.5BFO at all temperatures investigated, despite the average structure differences at room temperature. Small and large box modeling of the PDFs, complemented with DFT calculations, support the presence of both tetragonal and rhombohedral distortion in BKT-0.25BFO, while only pseudorhombohedral distortions are found in BKT-0.5BFO. The presence of both tetragonal and rhombohedral polar nanoregions (PNRs) in a pseudocubic average matrix phase are suggested to be responsible for the optimal piezoelectric properties found for the composition BKT-0.25BFO.

ACKNOWLEDGMENTS

This work was supported by the Research Council of Norway through the SYNKNØYT project 228571/F50. Computational resources were provided by Uninett Sigma2 through the project NN9264K. We thank Andrew Fitch for valuable assistance at beamline ID22 at ESRF.

REFERENCES

[1] E.T. Wefring, M.A. Einarsrud, T. Grande, Electrical conductivity and thermopower of (1-*x*)$BiFeO_3$ - *x*$Bi_{0.5}K_{0.5}TiO_3$ (*x* = 0.1, 0.2) ceramics near the ferroelectric to paraelectric phase transition, Phys. Chem. Chem. Phys. 17(14) (2015) 9420-9428.
[2] E.T. Wefring, F.H. Schader, K.G. Webber, M.A. Einarsrud, T. Grande, Electrical conductivity and ferroelastic properties of Ti-substituted solid solutions (1-*x*)$BiFeO_3$ - *x*$Bi_{0.5}K_{0.5}TiO_3$, J. Eur. Ceram. Soc. 36(3) (2016) 497-506.
[3] H. Matsuo, Ferroelectric properties and domain structures of $(Bi_{0.5}K_{0.5})TiO_3$-$BiFeO_3$ ceramics, Trans. Mat. Res. Soc. Japan 2(36) (2011) 285-288.

[4] T. Ozaki, H. Matsuo, Y. Noguchi, M. Miyayama, S. Mori, Microstructures related to ferroelectric properties in $(Bi_{0.5}K_{0.5})TiO_3$–$BiFeO_3$, Jpn. J. Appl. Phys. 49(9) (2010) 09MC05.
[5] M.I. Morozov, M.-A. Einarsrud, T. Grande, Atmosphere controlled conductivity and Maxwell-Wagner relaxation in $Bi_{0.5}K_{0.5}TiO_3$–$BiFeO_3$ ceramics, J. Appl. Phys. 115(4) (2014) 044104.
[6] M.I. Morozov, M.-A. Einarsrud, T. Grande, Control of conductivity and electric field induced strain in bulk $Bi_{0.5}K_{0.5}TiO_3$–$BiFeO_3$ ceramics, Appl. Phys. Lett. 104(12) (2014) 122905.
[7] M.I. Morozov, M.-A. Einarsrud, T. Grande, Polarization and strain response in $Bi_{0.5}K_{0.5}TiO_3$-$BiFeO_3$ ceramics, Appl. Phys. Lett. 101(25) (2012) 252904.
[8] M.I. Morozov, M.A. Einarsrud, T. Grande, D. Damjanovic, Lead-free relaxor-like $0.75Bi_{0.5}K_{0.5}TiO_3$ – $0.25BiFeO_3$ ceramics with large electric field-induced strain, Ferroelectrics 439(1) (2012) 88-94.
[9] J. Shieh, K.C. Wu, C.S. Chen, Switching characteristics of MPB compositions of $(Bi_{0.5}Na_{0.5})TiO_3$-$BaTiO_3$-$(Bi_{0.5}K_{0.5})TiO_3$ lead-free ferroelectric ceramics, Acta Mater. 55(9) (2007) 3081-3087.
[10] J. Rödel, W. Jo, K.T.P. Seifert, E.M. Anton, T. Granzow, D. Damjanovic, Perspective on the development of lead-free piezoceramics, J. Am. Ceram. Soc. 92(6) (2009) 1153-1177.
[11] V.V. Shvartsman, D.C. Lupascu, Lead-free relaxor ferroelectrics, J. Am. Ceram. Soc. 95(1) (2012) 1-26.
[12] G. Catalan, J.F. Scott, Physics and applications of bismuth ferrite, Adv. Mater. 21(24) (2009) 2463-2485.
[13] F. Kubel, H. Schmid, Structure of a ferroelectric and ferroelastic monodomain crystal of the perovskite $BiFeO_3$, Acta Crystallogr. Sect. B: Struct. Sci. 46 (1990) 698-702.
[14] T. Rojac, A. Bencan, B. Malic, G. Tutuncu, J.L. Jones, J.E. Daniels, D. Damjanovic, $BiFeO_3$ ceramics: processing, electrical, and electromechanical properties, J. Am. Ceram. Soc. 97(7) (2014) 1993-2011.
[15] J. Wang, J.B. Neaton, H. Zheng, V. Nagarajan, S.B. Ogale, B. Liu, D. Viehland, V. Vaithyanathan, D.G. Schlom, U.V. Waghmare, N.A. Spaldin, K.M. Rabe, M. Wuttig, R. Ramesh, Epitaxial $BiFeO_3$ multiferroic thin film heterostructures, Science 299(5613) (2003) 1719-1722.
[16] D.C. Arnold, K.S. Knight, F.D. Morrison, P. Lightfoot, Ferroelectric-paraelectric transition in BiFeO3: crystal structure of the orthorhombic beta phase, Phys. Rev. Lett. 102(2) (2009) 027602.
[17] D. Lebeugle, D. Colson, A. Forget, M. Viret, Very large spontaneous electric polarization in $BiFeO_3$ single crystals at room temperature and its evolution under cycling fields, Appl. Phys. Lett. 91(2) (2007) 022907.
[18] J. Neaton, C. Ederer, U. Waghmare, N. Spaldin, K. Rabe, First-principles study of spontaneous polarization in multiferroic $BiFeO_3$, Phys. Rev. B 71(1) (2005) 014113.
[19] S.M. Selbach, T. Tybell, M.-A. Einarsrud, T. Grande, The ferroic phase transitions of $BiFeO_3$, Adv. Mater. 20(19) (2008) 3692-3696.
[20] S.M. Selbach, T. Tybell, M.A. Einarsrud, T. Grande, Phase transitions, electrical conductivity and chemical stability of $BiFeO_3$ at high temperatures, J. Solid State Chem. 183(5) (2010) 1205-1208.
[21] Y. Wang, J.E. Saal, P.P. Wu, J.J. Wang, S.L. Shang, Z.K. Liu, L.Q. Chen, First-principles lattice dynamics and heat capacity of $BiFeO_3$, Acta Mater. 59(10) (2011) 4229-4234.
[22] R.D. Shannon, Revised effective ionic-radii and systematic studies of interatomic distances in halides and chalcogenides, Acta Crystallogr., Sect. A 32(SEP1) (1976) 751-767.
[23] Y. Hiruma, R. Aoyagi, H. Nagata, T. Takenaka, Ferroelectric and piezoelectric properties of $(Bi_{1/2}K_{1/2})TiO_3$ ceramics, Jpn. J. Appl. Phys. 44(7A) (2005) 5040-5044.
[24] Y. Hiruma, H. Nagata, T. Takenaka, Grain-size effect on electrical properties of $(Bi_{1/2}K_{1/2})TiO_3$ ceramics, Jpn. J. Appl. Phys. 46(3A) (2007) 1081-1084.
[25] V.V. Ivanova, Kapyshev, A.G., Venevtsev, Yu.N., Zhdanov, G.S., X-ray determination of the symmetry of elementary cells of the ferroelectric materials $(K_{0.5}Bi_{0.5})TiO_3$ and $(Na_{0.5}Bi_{0.5})TiO_3$ and of high-temperature phase transitions in $(K_{0.5}Bi_{0.5})TiO_3$, Bull. Acad. Sci. USSR Phys. Ser. 26(3) (1962) 358-360.
[26] M. Otonicar, S.D. Skapin, B. Jancar, R. Ubic, D. Suvorov, Analysis of the phase transition and the domain structure in $K_{0.5}Bi_{0.5}TiO_3$ perovskite ceramics by in situ XRD and TEM, J. Am. Ceram. Soc. 93(12) (2010) 4168-4173.

[27] G. Burns, F.H. Dacol, Glassy polarisation behaviour in ferroelectric compounds $Pb(Mg_{1/3}Nb_{2/3})O_3$ and $Pb(Zn_{1/3}Nb_{2/3})O_3$, Solid State Commun. 48(10) (1983) 853-856.
[28] M. Otonicar, S.D. Skapin, M. Spreitzer, D. Suvorov, Compositional range and electrical properties of the morphotropic phase boundary in the $Na_{0.5}Bi_{0.5}TiO_3$-$K_{0.5}Bi_{0.5}TiO_3$ system, J. Eur. Ceram. Soc. 30(4) (2010) 971-979.
[29] B. Jiang, T. Ræder, D.-Y. Lin, T. Grande, S.M. Selbach, Structural disorder and coherence across the phase transitions of lead-free piezoelectric $Bi_{0.5}K_{0.5}TiO_3$ Chem. Mater. 30(8) (2018) 2631−2640.
[30] H. Matsuo, Y. Noguchi, M. Miyayama, M. Suzuki, A. Watanabe, S. Sasabe, T. Ozaki, S. Mori, S. Torii, T. Kamiyama, Structural and piezoelectric properties of high-density $(Bi_{0.5}K_{0.5})TiO_3$–$BiFeO_3$ ceramics, J. Appl. Phys. 108(10) (2010) 104103.
[31] J.M. Kim, Y.S. Sung, J.H. Cho, T.K. Song, M.H. Kim, H.H. Chong, T.G. Park, D. Do, S.S. Kim, Piezoelectric and dielectric properties of lead-free (1-x)$(Bi_{0.5}K_{0.5})$TiO3-x$BiFeO_3$ ceramics, Ferroelectrics 404(1) (2010) 88-92.
[32] S.M. Selbach, M.A. Einarsrud, T. Grande, On the thermodynamic stability of BiFeO3, Chem. Mater. 21(1) (2009) 169-173.
[33] B. Noheda, D.E. Cox, G. Shirane, J.A. Gonzalo, L.E. Cross, S.E. Park, A monoclinic ferroelectric phase in the $Pb(Zr_{1-x}Ti_x)O_3$ solid solution, Appl. Phys. Lett. 74(14) (1999) 2059-2061.
[34] B. Noheda, J.A. Gonzalo, L.E. Cross, R. Guo, S.E. Park, D.E. Cox, G. Shirane, Tetragonal-to-monoclinic phase transition in a ferroelectric perovskite: The structure of $PbZr_{0.52}Ti_{0.48}O_3$, Phys. Rev. B 61(13) (2000) 8687-8695.
[35] T. Takenaka, K. Maruyama, K. Sakata, $Bi_{1/2}Na_{1/2})TiO_3$–$BaTiO_3$ system for lead-free piezoelectric ceramics, Jpn. J. Appl. Phys. 30(9B) (1991) 2236-2239.
[36] C.G. Xu, D.M. Lin, K.W. Kwok, Structure, electrical properties and depolarization temperature of (Bi0.5Na0.5)TiO3-BaTiO3 lead-free piezoelectric ceramics, Solid State Sci. 10(7) (2008) 934-940.
[37] S. Swain, S.K. Kar, P. Kumar, Dielectric, optical, piezoelectric and ferroelectric studies of NBT-BT ceramics near MPB, Ceram. Int. 41(9) (2015) 10710-10717.
[38] B. Jiang, T. Grande, S.M. Selbach, Local structure of dsordered $Bi_{0.5}K_{0.5}TiO_3$ investigated by pair distribution function analysis and first-principles calculations, Chem. Mater. 29(10) (2017) 4244-4252.
[39] E. Aksel, J.S. Forrester, J.C. Nino, K. Page, D.P. Shoemaker, J.L. Jones, Local atomic structure deviation from average structure of $Na_{0.5}Bi_{0.5}TiO_3$: Combined x-ray and neutron total scattering study, Phys. Rev. B 87(10) (2013) 104113.
[40] V.A. Shuvaeva, D. Zekria, A.M. Glazer, Q. Jiang, S.M. Weber, P. Bhattacharya, P.A. Thomas, Local structure of the lead-free relaxor ferroelectric$(K_xNa_{1-x})_{0.5}Bi_{0.5}TiO_3$, Phys. Rev. B 71(17) (2005) 174114.
[41] V. Petkov, Nanostructure by high-energy X-ray diffraction, Mater. Today 11(11) (2008) 28-38.
[42] V. Petkov, S.M. Selbach, M.A. Einarsrud, T. Grande, S.D. Shastri, Melting of Bi sublattice in nanosized $BiFeO_3$ perovskite by resonant X-Ray diffraction, Phys. Rev. Lett. 105(18) (2010) 185501.
[43] D. Hou, C. Zhao, A.R. Paterson, S. Li, J.L. Jones, Local structures of perovskite dielectrics and ferroelectrics via pair distribution function analyses, J. Eur. Ceram. Soc. 38(4) 971-987.
[44] H. Liu, J. Chen, L.L. Fan, Y. Ren, Z. Pan, K.V. Lalitha, J.G. Rodel, X.R. Xing, Critical role of monoclinic polarization rotation in high-performance perovskite piezoelectric materials, Phys. Rev. Lett. 119(1) (2017) 017601.
[45] H. Liu, J. Chen, L.L. Fan, Y. Ren, L. Hu, F.M. Guo, J.X. Deng, X.R. Xing, Structural evidence for strong coupling between polarization rotation and lattice strain in monoclinic relaxor ferroelectrics, Chem. Mater. 29(14) (2017) 5767-5771.
[46] V. Petkov, P.Y. Zavalij, S. Lutta, M.S. Whittingham, V. Parvanov, S. Shastri, Structure beyond Bragg: Study of V2O5 nanotubes, Phys. Rev. B 69(8) (2004) 6.
[47] V. Petkov, V. Buscaglia, M. Buscaglia, Z. Zhao, Y. Ren, Structural coherence and ferroelectricity decay in submicron- and nano-sized perovskites, Phys. Rev. B 78(5) (2008) 054107.
[48] S. Tripathi, V. Petkov, S.M. Selbach, K. Bergum, M.A. Einarsrud, T. Grande, Y. Ren, Structural coherence and ferroelectric order in nanosized multiferroic YMnO3, Phys. Rev. B 86(9) (2012) 8.

[49] A.C. Larson, R.B.V. Dreele, General Structure Analysis System technical manual, LANSCE, MS–H805 Los Almos National Laboratory LAUR (2000) 86-748.
[50] P. Juhas, T. Davis, C.L. Farrow, S.J.L. Billinge, PDFgetX3: a rapid and highly automatable program for processing powder diffraction data into total scattering pair distribution functions, J. Appl. Crystallogr. 46 (2013) 560-566.
[51] C.L. Farrow, P. Juhas, J.W. Liu, D. Bryndin, E.S. Bozin, J. Bloch, T. Proffen, S.J. Billinge, PDFfit2 and PDFgui: computer programs for studying nanostructure in crystals, J. Phys. Condens. Matter 19(33) (2007) 335219.
[52] M.G. Tucker, D.A. Keen, M.T. Dove, A.L. Goodwin, Q. Hui, RMCProfile: reverse Monte Carlo for polycrystalline materials, J. Phys. Condens. Matter 19(33) (2007) 335218.
[53] G. Kresse, J. Furthmuller, Efficient iterative schemes for ab initio total-energy calculations using a plane-wave basis set, Phys. Rev. B 54(16) (1996) 11169-11186.
[54] G. Kresse, D. Joubert, From ultrasoft pseudopotentials to the projector augmented-wave method, Phys. Rev. B 59(3) (1999) 1758-1775.
[55] J.P. Perdew, A. Ruzsinszky, G.I. Csonka, O.A. Vydrov, G.E. Scuseria, L.A. Constantin, X.L. Zhou, K. Burke, Restoring the density-gradient expansion for exchange in solids and surfaces, Phys. Rev. Lett. 100(13) (2008) 136406.
[56] J.P. Perdew, K. Burke, M. Ernzerhof, Generalized gradient approximation made simple, Phys. Rev. Lett. 77(18) (1996) 3865-3868.
[57] I. Sosnowska, W. Schaffer, W. Kockelmann, K.H. Andersen, I.O. Troyanchuk, Crystal structure and spiral magnetic ordering of $BiFeO_3$ doped with manganese, Appl. Phys. A 74 (2002) S1040-S1042.
[58] B. Jiang, S.M. Selbach, Local and average structure of Mn- and La-substituted BiFeO3, J. Solid State Chem. 250 (2017) 75-82.
[59] N.A. Spaldin, A beginner's guide to the modern theory of polarization, J. Solid State Chem. 195 (2012) 2-10.
[60] M.S. Senn, D.A. Keen, T.C.A. Lucas, J.A. Hriljac, A.L. Goodwin, Emergence of long-range order in $BaTiO_3$ from local symmetry-breaking distortions, Phys. Rev. Lett. 116(20) (2016) 207602.
[61] I.K. Jeong, Temperature evolution of short- and medium-range ionic correlations in relaxor ferroelectric $[Pb(Zn_{1/3}Nb_{2/3})O_3]_{(1-x)}$ $[PbTiO_3]_x$ (x=0.05, 0.12), Phys. Rev. B 79(5) (2009) 052101
[62] M. Gröting, S. Hayn, K. Albe, Chemical order and local structure of the lead-free relaxor ferroelectric $Na_{1/2}Bi_{1/2}TiO_3$, J. Solid State Chem. 184(8) (2011) 2041-2046.
[63] M. Gröting, K. Albe, Comparative study of A-site order in the lead-free bismuth titanates $M_{1/2}Bi_{1/2}TiO_3$ (M=Li, Na, K, Rb, Cs, Ag, Tl) from first-principles, J. Solid State Chem. 213 (2014) 138-144.
[64] T. Grande, J.R. Tolchard, S.M. Selbach, Anisotropic thermal and chemical expansion in Sr-substituted $LaMnO_{3+\delta}$: implications for chemical strain Relaxation, Chem. Mater. 24(2) (2012) 338-345.
[65] J.H. Hildebrand, R.L. Scott, Regular Solutions, Englewood Cliffs, NJ (1962).
[66] S. Stølen, T. Grande, Chemical thermodynamics of materials: macroscopic and microscopic aspects, John Wiley & Sons, Chichester, 2003.

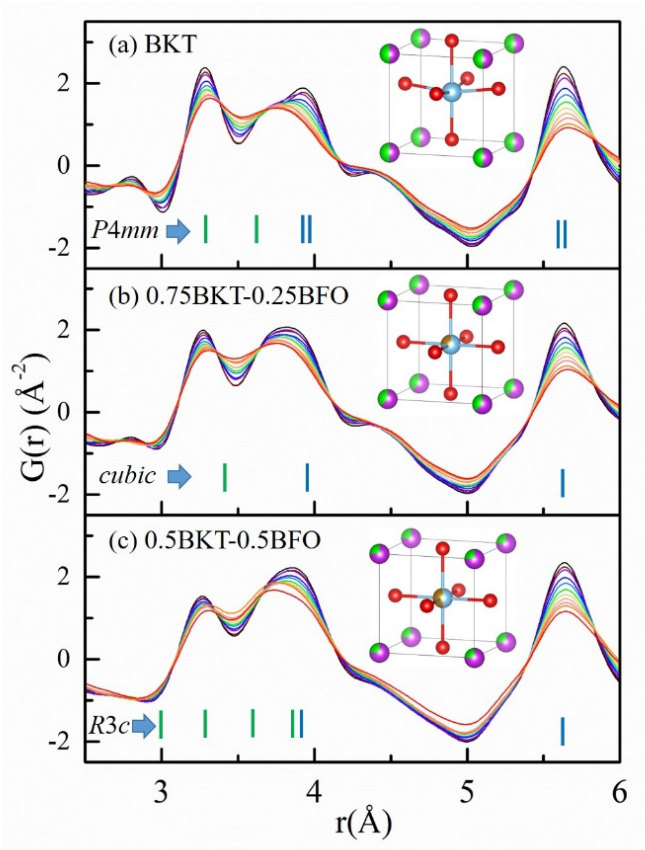

Figure 1. Pair distribution functions (PDF) of (a) BKT, (b) BKT-0.25BFO and (c) BKT-0.5BFO from room temperature (black) to 773 K (red) with 50 K intervals. The insets show the corresponding average structures from conventional X-ray diffraction. The ticks indicate (a) the Bi/K-Ti(short), Bi/K-Ti(long) and A/B-A/B bond distances in tetragonal BKT; (b) A-B and A/B-A/B bond distances in the cubic perovskite structure; and (c) four Bi-Fe peaks and Bi-Bi bond distances in rhombohedral *R*3*c* $BiFeO_3$.

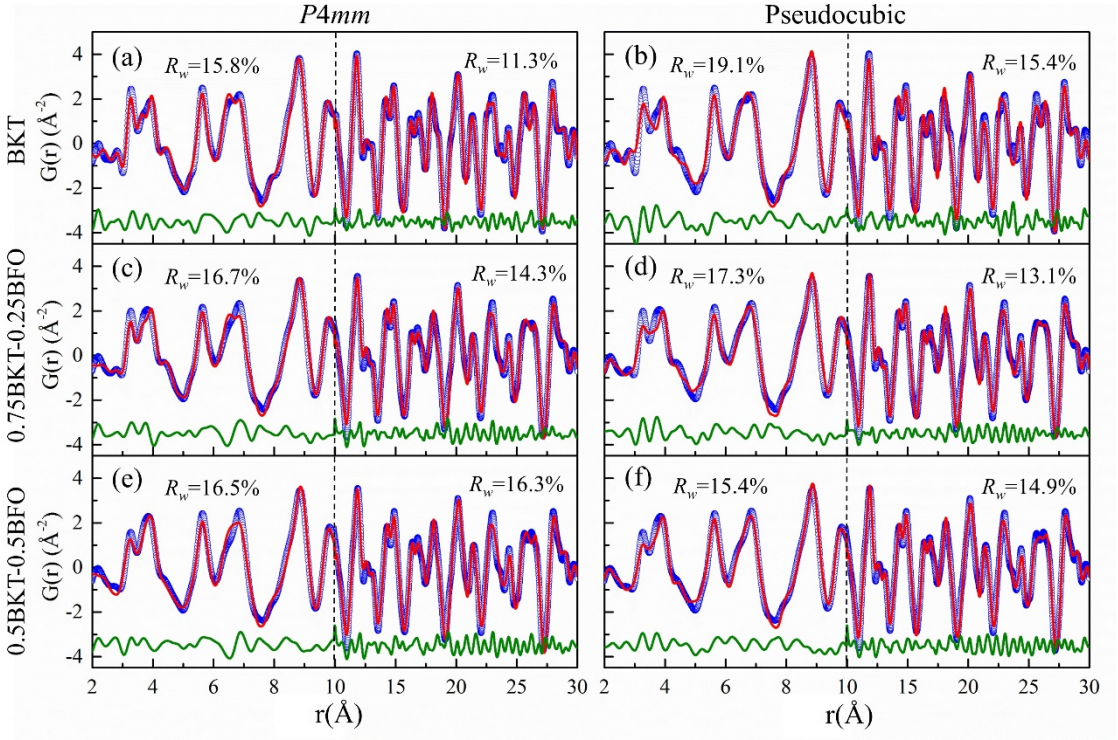

Figure 2. Room temperature PDFs of BKT, BKT-0.25BFO and BKT-0.5BFO fitted to tetragonal *P*4*mm* (a, c, e) and pseudocubic (b, d, f) models for the local r =1.5-10 Å and the intermediate r = 10-30 Å ranges. The reliability factors R_w are included in the panels. Open circles: experimental data; red solid lines: calculated data; the green difference curves shown below each plot.

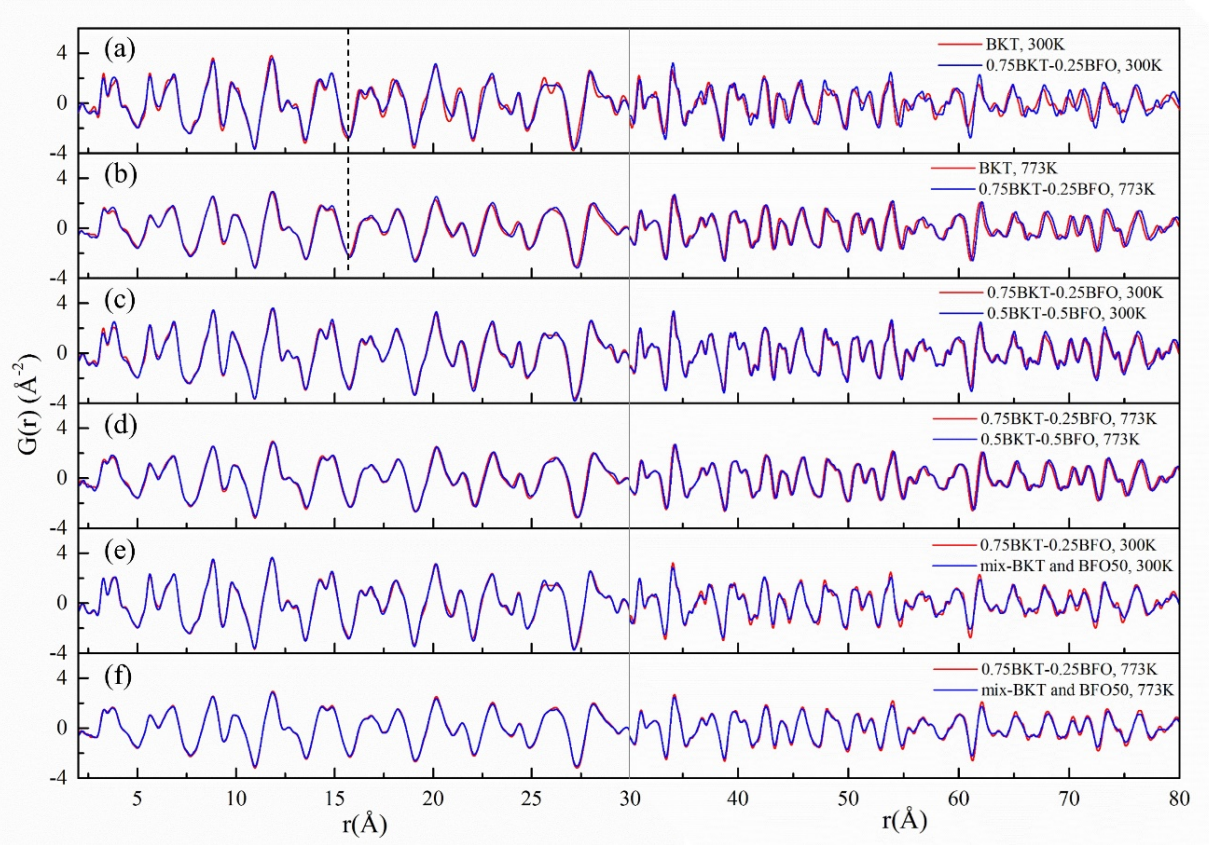

Figure 3. PDF patterns collected at 300 and 773 K, comparing: BKT and BKT-0.25BFO at (a) 300 K and (b) 773 K; BKT-0.25BFO and BKT-0.5BFO at (c) 300 K and (d) 773 K; BKT-0.25BFO and mixed BKT and BKT-0.5BFO at (e) 300 K and (f) 773 K. The mixed BKT and BKT-0.5BFO PDF patterns are obtained by averaging the BKT and BKT-0.5BFO patterns.

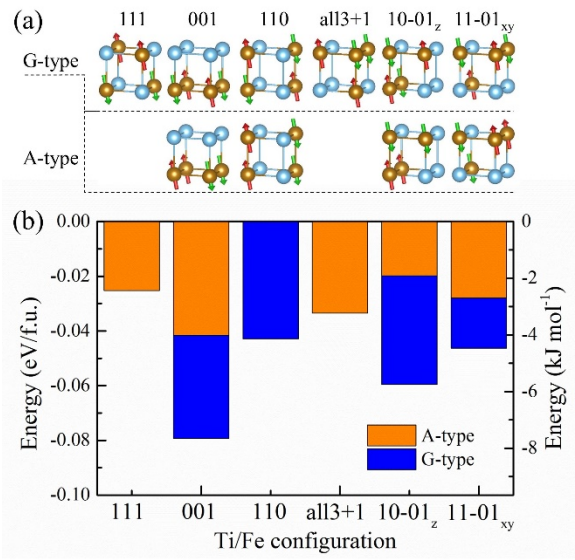

Figure 4. (a) 2×2×2 perovskite supercell configurations of BKT-0.5BFO ($Bi_6K_2Ti_4Fe_4O_{24}$). The simple cubic sublattice of B-site atoms is shown with Ti as blue and Fe as purple, with arrows on Fe atoms showing the antiferromagnetic spin up (red) and down (green) order. The labels describe the local A-site cation ordering following Gröting and Albe [62, 63]. (b) Relative energy per formula unit of BKT-0.5BFO ($Bi_{0.75}K_{0.25}Ti_{0.5}Fe_{0.5}O_3$) of the investigated B-site (Ti/Fe) configurations in BKT-0.5BFO for pseudocubic structure. The relative energy of A-type antiferromagnetic Fe^{3+} sublattice is shown in orange, and G-type antiferromagnetic Fe^{3+} sublattice in blue. The zero-energy level is set as the energy of the A-type all3+1 structure which has the highest energy per formula unit.

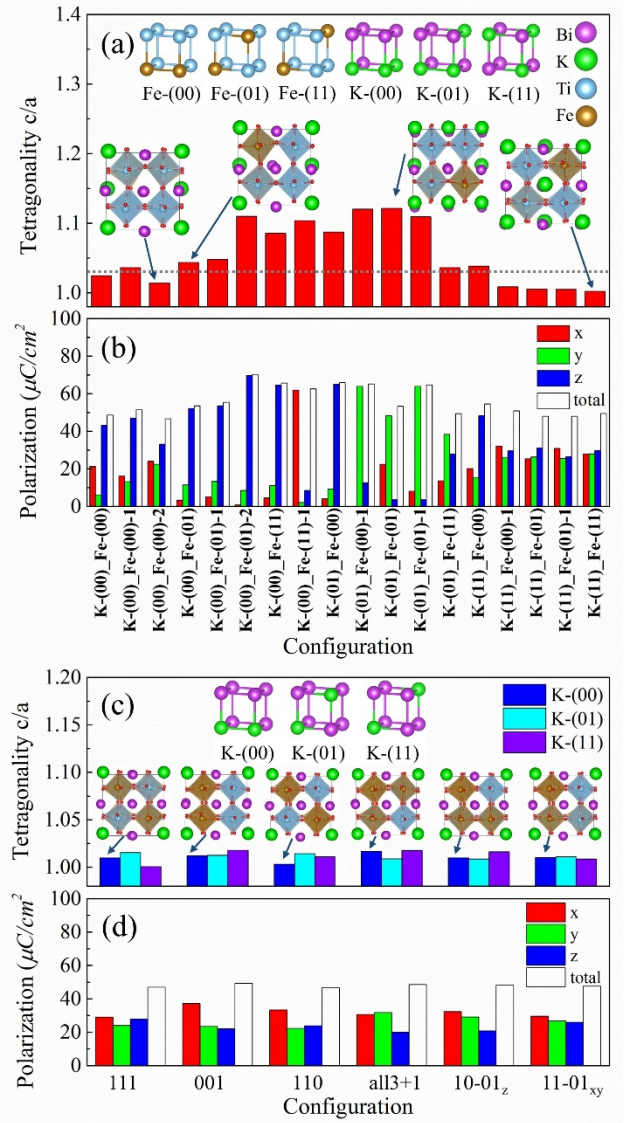

Figure 5. (a) Tetragonality *c*/*a* for fully relaxed structures of different cation configurations in 2x2x2 supercells of BKT-0.25BFO. The horizontal dashed line depicts an estimated boundary between tetragonal and pseudocubic structures. The insets show the configurations of A-site and B-site, and selected final structures. (b) Polarization (P_s) of BKT-0.25BFO for different configurations from a point charge model. Red, green, blue and white bars represent *x*-, *y*- and *z*- components of the polarization and the total polarization, respectively. (c) Tetragonality *c*/*a* for fully relaxed structures of BKT-0.5BFO. The insets show the A-site configurations and selected final structures. (b) Polarization (P_s) of BKT-0.50BFO for different configurations

from a point charge model. Red, green, blue and wgite bars represent *x*-, *y*- and *z*- components of the polarization and the total polarization, respectively.

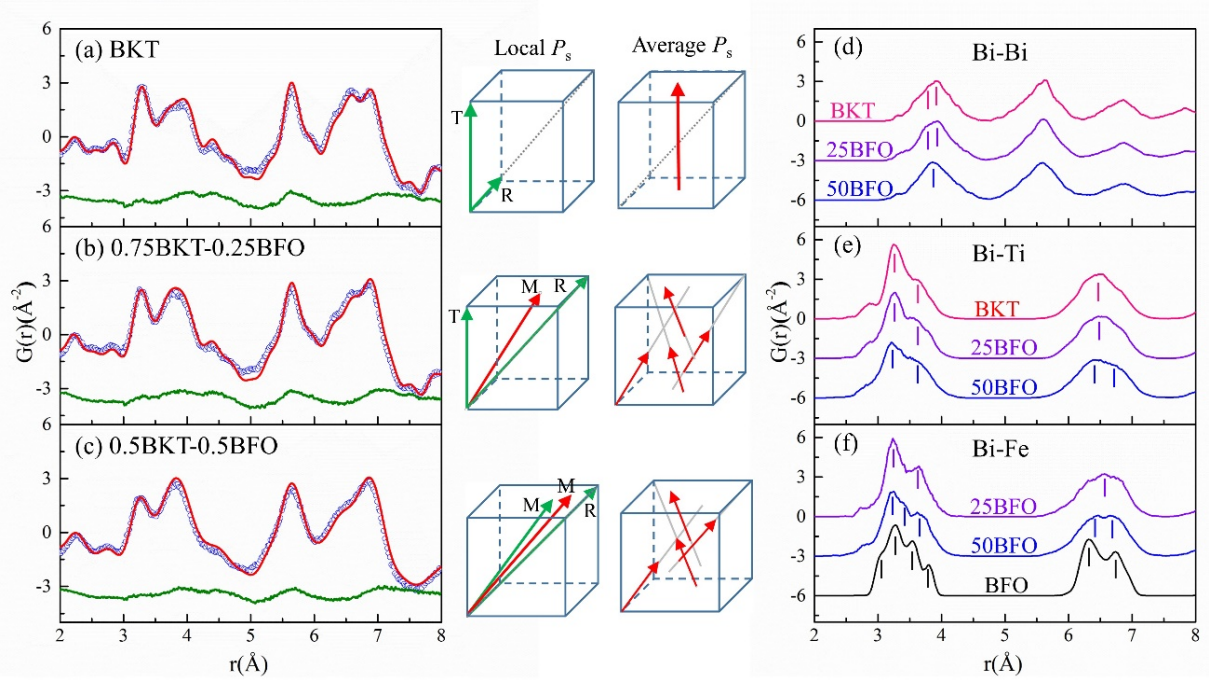

Figure 6. Experimental room temperature PDFs fitted by RMC simulations with 12×12×12 supercells: (a) BKT, (b) BKT-0.25BFO and (c) BKT-0.5BFO Bi-based partial PDFs: (d) Bi-Bi, (e) Bi-Fe and (f) Bi-Fe. Proposed corresponding local and average structure models with polarization directions indicated are shown on the middle panels for T(tetragonal), M (Monoclinic), R(rhombohedral) regions.

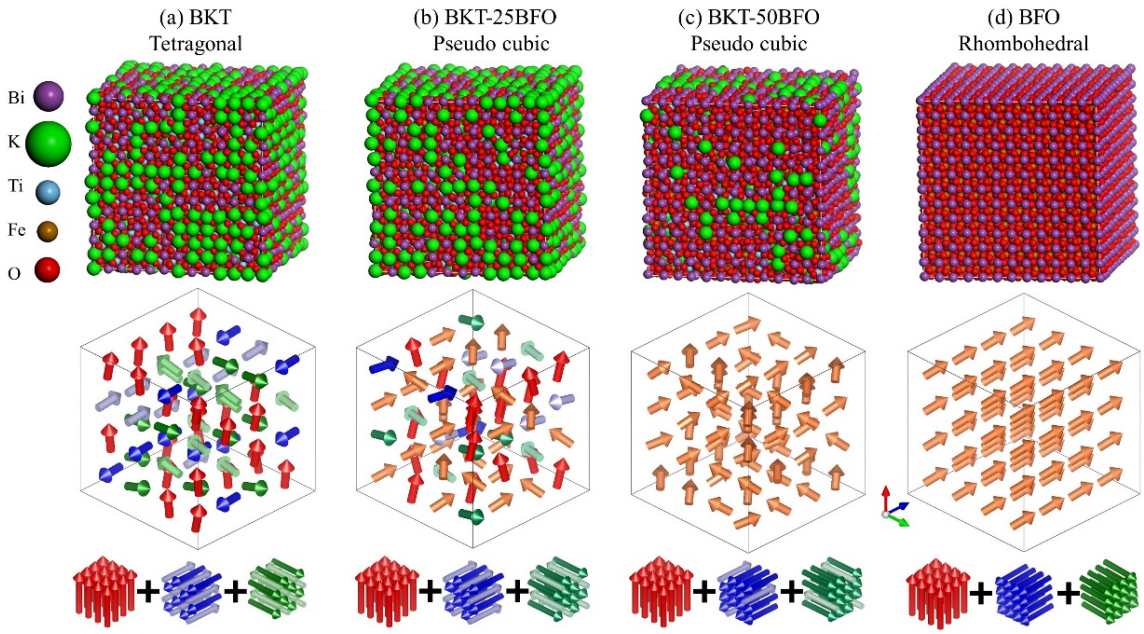

Figure 7. RMC derived structural configurations for (a) BKT, (b) BKT-0.25BFO, (c) BKT-0.5BFO and (d) BFO, with proposed mesoscopic polar vector models for the different compounds illustrated below.